Ultrathin freestanding membranes of ZrO_2 with metastable structures and strain-dependent electrical properties

Yufan Shen [1], Kousuke Ooe [2,3], Kazuki Shitara [3], Shunsuke Kobayashi [3], Takeshi Yoshimura [4], Tomoaki Yamada [5,6], Lingling Xie [1], Yuichi Shimakawa [1], and Daisuke Kan [1,7,*]

[1] *Institute for Chemical Research, Kyoto University, Uji, Kyoto, Japan*

[2] *School of Physics and Astronomy, Monash University, Clayton VIC 3800, Australia*

[3] *Nanostructures Research Laboratory, Japan Fine Ceramics Center, Nagoya, Japan*

[4] *Graduate School of Engineering, Department of Physics and Electronics, Osaka Metropolitan University, Sakai, Osaka, Japan*

[5] *Department of Energy Engineering, Nagoya University, Nagoya, Japan*

[6] *MDX Research Center for Element Strategy, International Research Frontiers Initiative, Institute of Science Tokyo, Yokohama, Japan*

[7] *Japan Science and Technology Agency (JST), Kawaguchi, Saitama 332-0012, Japan*

(Received 23 September 2024; accepted 31 January 2025; published 28 February 2025)

Fabricating and investigating freestanding membranes of materials are key approaches for exploring the intrinsic properties of those materials, even in their metastable phases stabilized by external factors. In this study, we fabricated freestanding ZrO_2 membranes with metastable crystal structures by exfoliating ZrO_2 (ZO) epitaxial layers from $ZrO_2/La_{0.7}Sr_{0.3}MnO_3/SrTiO_3$ heterostructures. By combining the results of first-principles calculations, we found that with increasing thickness up to 15 nm, ZO membranes undergo structural relaxation from the metastable tetragonal structure to a metastable orthorhombic one. In addition, the dielectric constant of the tetragonal ZO is susceptible to the out-of-plane lattice constant of the ZO layer. The change in out-of-plane interplanar distance, which primarily stems from the strain release associated with the exfoliation of ZO layers, leads to an increase in the dielectric constant (to ~ 25). ZO membranes with high dielectric constants could be utilized in energy storage capacitors.

DOI: 10.1103/PhysRevMaterials.9.024411

I. INTRODUCTION

Recent demonstrations of the fabrication of complex oxides into freestanding ultrathin crystalline membranes have revealed their potential to be a promising platform for exploring materials' intrinsic properties and device applications [1–6]. Significantly, membranes fabricated by exfoliating epitaxial films of metal oxides from the substrates can be stacked on various materials that structurally differ from the exfoliated ones, enabling the fabrications of stacking structures and heterostructures that cannot be made by conventional film growth techniques. This feature of freestanding membrane specimens has led to the discovery of intriguing physical properties not seen in epitaxial films, such as superelasticity and twisted-angle-dependent vortex patterns of ferroelectric polarization [7,8].

Another important characteristic of membrane specimens is that they are free of substrate-induced and interfacial effects, such as strain effects that often impact thin films' structural and physical properties, especially when the films are only a few nanometers thick. Fabricating and investigating freestanding membranes, therefore, offer approaches to get insight into the intrinsic properties of materials even in their metastable phases. Recently, the fabrications of crystalline membranes of metastable and ferroelectric hafnia ($Hf_{0.5}Zr_{0.5}O_2$, HZO) with spontaneous polarizations of 10 to 20 $\mu C/cm^2$ have been demonstrated [9–11]. Interestingly, hafnia membranes with thicknesses down to 1 nm can maintain the crystal structure of metastable and ferroelectric rhombohedral phases. As the thickness increases to 5 nm, the rhombohedral phase transforms into another metastable orthorhombic phase without deteriorating ferroelectricity [10]. These results reveal the significance of the metastable rhombohedral phase in the scale-free ferroelectricity of hafnia and provide critical insights into the formation mechanism and phase stability of the metastable hafnia.

Like hafnia, the fluorite zirconia ZrO_2 (ZO) also displays various polymorphs whose properties depend on their crystal structures and external factors like strain and interfacial layer [12–14]. The most stable phase of ZO is monoclinic, which is regarded as a nonpolar dielectric. Among metastable polymorphs, the orthorhombic phase could be (anti-)polar, as shown from both experimental and theoretical investigations [12,14,15], and recent investigations have also shown that the metastable ferroelectric rhombohedral phase of ZO could be epitaxially stabilized [16–18]. Moreover, ZO in the form of films and freestanding membranes have been shown to undergo structural transformation from nonpolar to polar phases and vice versa under electric fields, for example, from the nonpolar tetragonal phase to the orthorhombic one [19,20] and from the orthorhombic phase to the monoclinic one [21,22]. Given the potential of ZO for various device applications [19,23,24], it is crucial to delineate the phase stability of

*Contact author: dkan@scl.kyoto-u.ac.jp

metastable phases of ZO and the influence of external factors on their properties, especially for ultrathin ZO films whose structures and properties are often influenced by extrinsic effects like substrate-induced strain and interfacial structural mismatches.

In this study, we fabricated freestanding ZO membranes with metastable crystal structures by exfoliating ZO layers from ZO/$La_{0.7}Sr_{0.3}MnO_3$(LSMO)/$SrTiO_3$(STO) epitaxial heterostructures. We found that with increasing thickness up to 15 nm-thick, ZO membranes undergo structural relaxation from the metastable tetragonal structure to a metastable orthorhombic one. In addition, we also found the dielectric constant of the tetragonal ZO to be susceptible to the out-of-plane lattice constant in the ZO layer. The out-of-plane lattice constant changes, which are mainly due to strain release associated with the exfoliation of ZO layers, are related to an increase in the dielectric constant (to ∼25), and ZO membranes with high dielectric constants could be utilized in energy storage capacitors.

II. EXPERIMENTAL SECTION

A. Epitaxial heterostructures and freestanding membranes fabrication

The epitaxial ZO/LSMO heterostructures were fabricated by pulsed laser deposition (PLD) system on TiO_2-terminated (100) STO substrates (Shinkosya Co., Japan).

LSMO layers were first deposited by ablating a ceramic target with a nominal cation composition of LSMO with the excimer laser (Coherent COMPex Pro 205 KrF, $\lambda = 248$ nm) with an energy density of 1.2 J/cm^2 and a repetition of 5 Hz. During the deposition of LSMO layers, the substrate temperature was kept at 700 °C, and the oxygen partial pressure was maintained at 100 mTorr. Subsequently, without breaking the vacuum of the PLD chamber, ZO layers were deposited at the substrate temperature of 800 °C and under the oxygen partial pressure of 75 mTorr, respectively. A ZrO_2 target was ablated with the laser with an energy density of 1.4 J/cm^2 and a repetition of 2 Hz. Prior to the LSMO and ZO depositions, the targets were pre-ablated for 30 seconds. After ZO and LSMO layer depositions, all samples were cooled to room temperature under the oxygen partial pressure of 75 mTorr. Freestanding ZO membranes were fabricated using essentially the same approach as those used for previously fabricating HZO membranes [10].

B. Structural characterization

X-ray $2\theta/\theta$ diffraction measurements were performed with a lab-source four-circle diffractometer (X'Pert MRD, PANalytical) using the Cu $K_{\alpha 1}$ radiation. For the top-view STEM observations of freestanding ZO membranes, membrane samples were transferred on a holey carbon film supported by a Cu grid. (S)TEM measurements were performed at 300 kV on an FEI Titan^3 80–300 FEG-TEM equipped with probe and imaging aberration correctors. For the HAADF STEM imaging, the probe forming semi-angle was set to be 15 mrad, and the HAADF detector collection angle was 20 to 200 mrad. To minimize image distortion due to sample-stage drift and improve the signal-to-noise ratio, ∼30 HAADF images were sequentially acquired with a fast dwell time of 500 ns/pixel with the same field-of-view. They were then spatially stacked and averaged.

We also performed plan-view observations of ZO epitaxial films. Thin foils for STEM observations were prepared using a wedge polishing technique. STEM observations were conducted on a plan-view of the ZO (5 nm)/LSMO film grown on an STO substrate using an aberration-corrected (CEOSGmbH) scanning transmission electron microscope (JEM-2400FCS, JEOL Ltd.). The electron energy loss (EEL) spectra were obtained using an EELspectrometer (GIF Continuum ER, Gatan, Inc.) attached to an aberration-corrected scanning transmission electron microscope (JEM-2400FCS, JEOL Ltd.), operating at 200 kV.

C. Electrical characterization

For characterizing epitaxial ZO films, the 45-nm-thick LSMO layer served as the bottom electrode, and the top electrodes of 50-nm-thick Au pads in diameters from 30 to 50 μm were thermally evaporated and patterned by a conventional lift-off process. For characterizing ZO membranes, metal-insulator-metal (MIM) capacitors whose junction area ranged from 10 to 100 μm^2 were fabricated by transferring ZO membranes on 3-nm-thick Pt as the bottom metal and by depositing 50-nm-thick Au top electrodes on top of the transferred membranes. Details of fabrication processes were provided in our previous report [10]. The P-E loops were obtained with ferroelectric testers (FCE-10 TOYO Corp and Precision multiferroic II ferroelectric tester Radiant Corp.). The capacitance was measured using the LCR meter (Agilent) with a measurement frequency of 10 kHz and an a.c. bias of 0.1 V. The energy storage density (ESD) was estimated using P-E curves in the first quadrant and based on ESD $= \int_{Pr}^{Pm} EdP$ in which P_m and P_r stand for maximum and remanent polarization, respectively, and E stands for the electrical field. The efficiency (η) is calculated based on $\eta = \text{EDS}/\int_0^{Pm} EdP$ with the hysteresis area responsible for the η loss (hysteresis loss).

D. First-principles calculations

First-principles calculations were performed to evaluate structural energy as a function of thickness for the tetragonal and orthorhombic ZO. At first, tetragonal and orthorhombic bulk ZO crystals were calculated. Ultrathin film models of tetragonal-(001), tetragonal-(101), orthorhombic-(001), and orthorhombic-(111) are created by orienting ZO crystals along each direction. The vacuum layers whose thickness was set to 50 Å were introduced, and energy variations due to the thickness of the vacuum layer were confirmed to be less than 1 meV (Fig. S5 [25]). There are several candidate surface atomic layers, and we computed ∼1 nm (10 Å)-thick slab models with identical possible surface structures at the top and bottom. Figure S6 shows the most stable models with about 1 nm, and these models were used to evaluate the thickness dependence of structural energy [25]. First-principles calculations based on density functional theory (DFT) were conducted using the projector augmented-wave (PAW) method implemented in the VASP code [26–28]. The exchange-correlation term was treated with GGA-PBE for

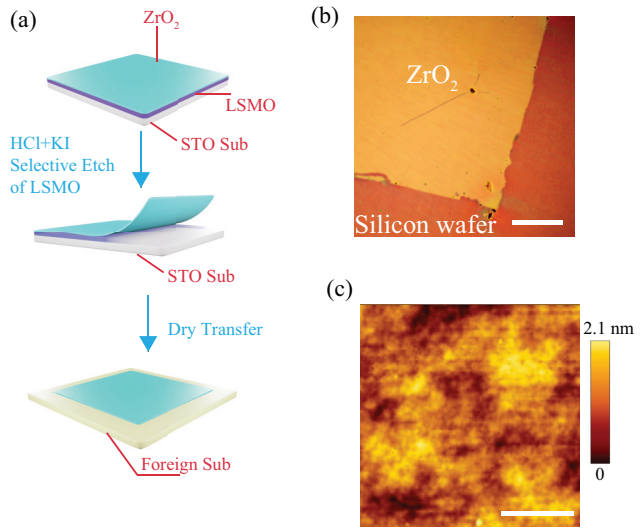

FIG. 1. Fabrication and structural characterization of ZO membranes. (a) Fabrication process of freestanding ZO membranes. (b) Optical image of fabricated 10-nm-thick ZO membrane. The scale bar denotes 0.5 mm. (c) Surface topography of 10-nm-thick ZO membrane characterized by AFM. The scale bars correspond to 1 μm.

solids [29]. The plane-wave cutoff energy was set to 550 eV. Integration in reciprocal spaces was performed with 0.3 $Å^{-1}$ grids. Dipole correction as implemented in VASP code, was used to cancel the dipole-dipole interaction between unit cells [30]. Structure optimization was conducted until all residual forces acting on each atom were less than 0.1 eV $Å^{-1}$. Lattice constants and atomic positions were relaxed for the crystal models, while internal coordinates of atoms were relaxed for slab models.

III. FABRICATION OF ZrO_2 MEMBRANES

Figure 1(a) schematically shows the fabrication processes of ZO membranes. ZO epitaxial films were exfoliated from (100) STO substrates by selectively etching LSMO sacrificing layers in ZO/LSMO/STO heterostructures deposited by PLD. After fully etching LSMO sacrificing layers in hydrochloric acid solutions with potassium iodide as an antioxidant [31,32], ZO membranes are transferred to foreign substrates, such as SiO_2-coated Si wafers, using a conventional dry transfer method [33]. The optical image of the 10-nm-thick ZO membrane transferred on a SiO_2/Si substrate is shown in Fig. 1(b). The transferred membranes maintain almost the same contour as the square one of the STO substrate. The boundary between the transferred membrane and SiO_2/Si substrate is obvious and no apparent cracks are seen in the membranes. Figure 1(c) shows the typical surface topography of the 10-nm-thick ZO membrane characterized by atomic force microscopy (AFM), confirming that the membrane has a smooth surface whose root mean square (RMS) roughness is as low as 0.3 nm. It should be also mentioned that the 1-nm-thick membrane has a smooth surface with RMS roughness as low as 0.38 nm (Fig. S1 [25]), validating our transfer method.

IV. CRYSTAL STRUCTURES AND THEIR DISTRIBUTION IN ZrO_2 MEMBRANES

To identify crystal structures and delineate correlations between their distribution and strain relaxation in ZO membranes, we employed top-view HAADF imaging in STEM for ZO membranes transferred on TEM grids. We focused on ZO membranes thinner than 10 nm. We found that ZO membranes consist of grains with tetragonal and orthorhombic structures. Figure 2 shows the HAADF-STEM images and corresponding simulated diffraction patterns of grains with identified structures, which can be sorted as (101)- and (001)-oriented tetragonal ones (t-(101) and t-(001)) and (111)- and (001)-oriented orthorhombic (o-(111)) and o-(001)). While the grains in Fig. 2(a) apparently have a hexagonal Zr arrangement, their simulated diffraction patterns differ from those expected from the (111)-oriented cubic and rhombohedral structures that have the ideal hexagonal Zr arrangement (Fig. S2 [25]). Some weak reflections, such as -102 and 10–2 spots (Fig. S2 [25]), can be reproduced only by a structural model of the t-(101), not by structural models of cubic and rhombohedral structures (Fig. S2 [25]). Therefore grains with the (quasi-) hexagonal Zr lattice in Fig. 2(a) can be identified as t-(101). The Zr arrangement in Fig. 2(b) and the corresponding simulated diffraction pattern match well with those expected from the t-(001) structures. On the other hand, the HAADF-STEM images in Figs. 2(c) and 2(d) show periodic modulations in Zr-Zr distances, which match well with those expected from the (111)- and (001)-oriented orthorhombic structures. The simulated diffraction patterns obtained from the HAADF-STEM images in Figs. 2(c) and 2(d) are also well reproduced from the o-(111) and o-(001) structural models, ensuring our phase identification.

Interestingly, the distribution of the identified phases in Fig. 2 strongly depends on the thickness of the ZO membranes. Figures 3 and S3 show the results of phase distribution analysis of 1-, 5-, and 10-nm-thick membranes, which were obtained from grains (circled ones in the figures) whose Zr arrangements can be atomically resolved and structural phases can be identified. As shown in Figs. 3(a)–3(c) and Fig. S3 [25], more than 90% of the grains (whose structures can be identified) in the 1-nm and 5-nm-thick membranes have a tetragonal structure. The majority of them are oriented along the [101] direction, while a minority are oriented along the [001] direction. The selected area electron diffraction (SAED) patterns of these membranes can be regarded as a combination of diffraction patterns of the t-(101) and t-(001) structures, confirming our structural phase identification and distribution analysis [Fig. 3(b)]. We also note that some t-(101) grains in the 1-nm-thick membranes exhibit no superstructure spots characteristic of the tetragonal structure in their simulated diffraction patterns [Fig. S3(a)], implying a possible coexistence of either (111)-oriented rhombohedral or cubic phase and the tetragonal one (Fig. S3 [25]). Although precisely identifying structural phases in the ultrathin ZO membranes requires further investigation, our results indicate that grains having (quasi-) hexagonal Zr lattices form on LSMO layers at the initial stage of epitaxial growth of ZO layers through interfacial structural matching. Similar interfacial structural matching is seen for epitaxial growth of

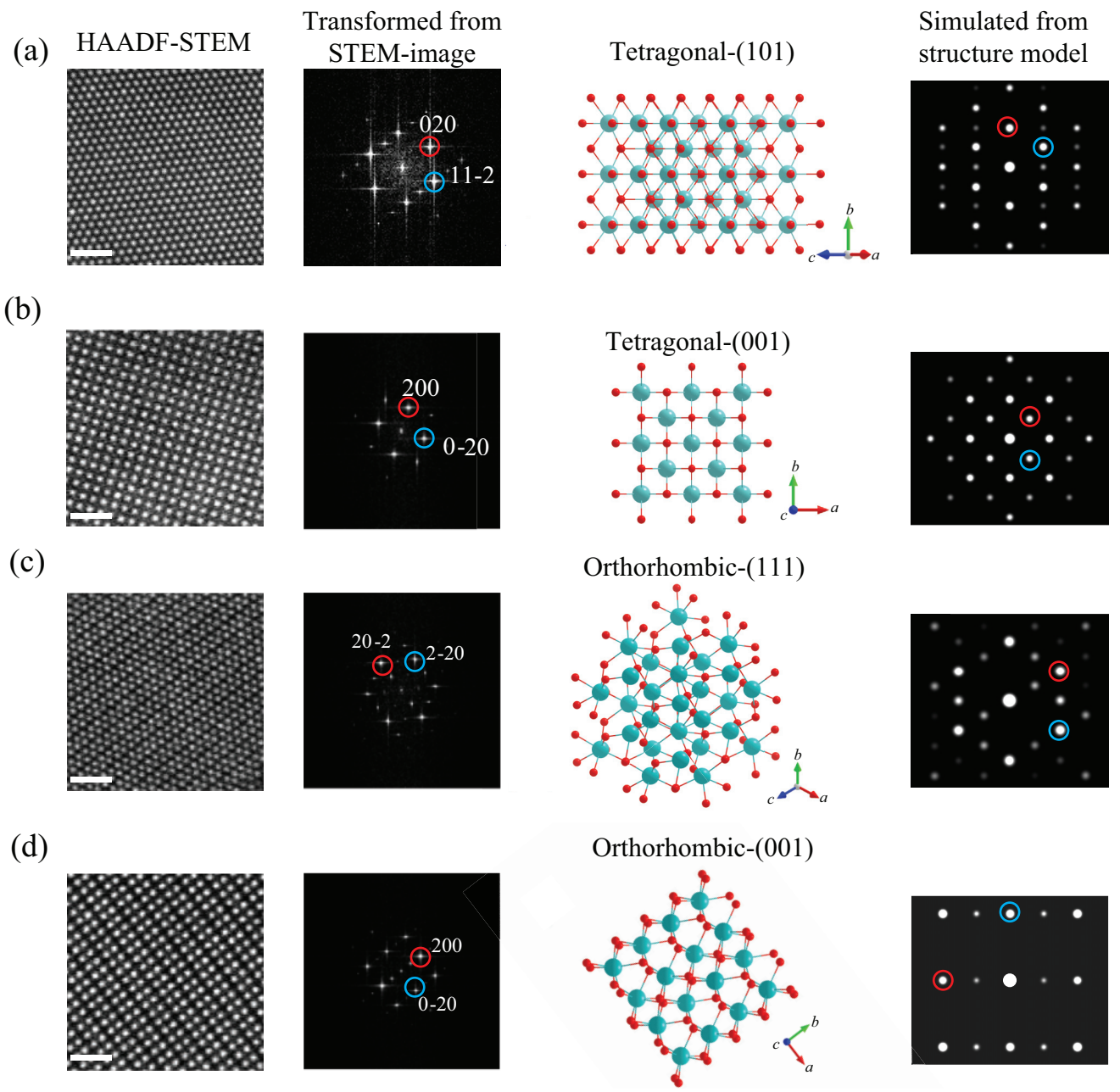

FIG. 2. Crystal structure identification in ZO membranes. Top-view HAADF-STEM images, crystal structure models, and diffraction patterns transformed/simulated from HAADF-STEM images and structural models of (a) (101)-oriented tetragonal structure, (b) (001)-oriented tetragonal one, (c) (111)-oriented orthorhombic one, and (d) (001)-oriented orthorhombic one. In the HAADF-STEM images, the scale bars correspond to 1 nm. Corresponding reflections in the diffraction patterns transformed/simulated from HAADF-STEM images and structural models are circled.

$Hf_{0.5}Zr_{0.5}O_2$ on LSMO layers [10,34,35]. Interestingly, the top-view HAADF-STEM observation for the 5-nm-thick ZO epitaxial film ensures the existence of grains having the t-(101) structure (Fig. S4 [25]). This implies that the metastable polymorphs of ZO are grown through the interfacial structural matching and that once they formed, they should be stable enough that the metastable polymorphs remain in membrane forms after ZO epitaxial films are exfoliated.

With further increasing thickness, the tetragonal structure transforms to another metastable orthorhombic phase. Figures 3(d)–3(f) show the top-view HAADF-STEM image and phase identification results for the 10-nm-thick ZO membranes. The membranes are found to consist of a mixture of grains having the t-(101), t-(001), o-(111) and o-(001). The coexistence of the tetragonal and orthorhombic grains is further confirmed by the SAED pattern in Fig. 3(e). In contrast to the thinner membranes, the percentage of the tetragonal grains in the 10-nm-thick membranes is reduced to 50%, indicating that the metastable tetragonal phase transforms into another metastable orthorhombic one through structural energy relaxation. It should also be noted that no grains with the most stable monoclinic phase are detected in the membranes

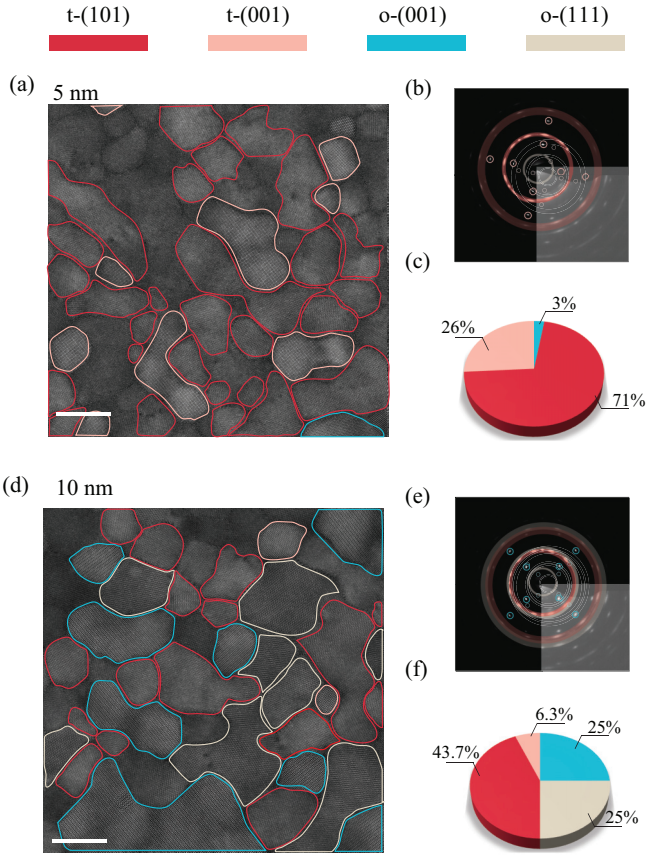

FIG. 3. Structural phase distribution in ZO membranes. (a) Top-view HAADF-STEM image, (b) SAED pattern, and (c) structural phase distribution for the 5-nm-thick ZO membrane. (d) Top-view HAADF-STEM image, (e) SAED pattern, and (f) structural phase distribution for the 10-nm-thick ZO membrane. The red, pink, blue, and beige colors, respectively, correspond to t-(101), t-(001), o-(001), and o-(111). The scale bars in (a) and (d) denote 10 nm. In (a) and (d), the grains not circled are ones whose Zr arrangements were not atomically resolved, and structural phases could not be identified, possibly due to slight misalignment between the incident electron beam and grain surfaces. Insets in (b) and (e) are the high-contrasted parts of the SAED.

thinner than 10 nm, which is in agreement with the XRD results in Fig. 1(d).

We also carried out first-principles calculations to get insight into the stability of the tetragonal and orthorhombic phases and their transformation in ZO membranes. First, our calculations confirmed that the orthorhombic bulk model of ZO is more stable by 26 meV per the ZO formula unit cell than the tetragonal one, which agrees well with the previous computational report [36]. Then, we constructed structural models of o-(001), o-(111), t-(001), and t-(101) membranes with vacuum layers installed (Figs. S5 and S6), and calculated their structural energies. Figure 4 shows the relative energies of these membrane models as a function of their thicknesses. Because the thicknesses of a single layer of the structural models differ depending on their structures and orientations (Fig. S6 [25]), the total thicknesses of the computed models are discrete and different between the computed models. The energies of all models decrease with increasing thickness because of the larger contribution of the surface for the thinner models. The t-(101) model is the most stable among the models we computed in the thickness region up to ∼5 nm, in contrast to the bulk model, whose orthorhombic structure is stable against the tetragonal one. In the thickness region of about 10 Å (corresponding to the one or two unit cells of the membrane models), the energy increases in the order $t-(101) < o-(111) < t-(001) = o-(001)$, as shown in Fig. 4(c). Interestingly, the energy difference between the t-(101) and other models decreases with increasing thickness. When the thickness reaches around 50 Å, the energies of the t-(101) and o-(001) models become very close, with t-(101) being slightly lower than the t-(001) model [Fig. 4(b)]. The computed energy diagram supports our structural phase distribution results that the metastable tetragonal phase transforms into another metastable orthorhombic one through structural energy relaxation. We also point out that while the o-(111) has the second lowest energy, it was not experimentally detected even in the 1 nm-thick membranes, implying that the LSMO layer stabilizes the hexagonal Zr lattices of ZO layers.

Figure 5 compares X-ray $2\theta/\theta$ diffraction patterns for epitaxial films and freestanding membranes of ZO with thicknesses of 5, 10, and 15 nm. For the epitaxial films, in addition to the (001) reflections from the LSMO sacrificing layers and STO substrates, clear reflections at 2θ to 30°, which can be indexed as either o-(111) or t-(101) [37,38] according to the STEM-based phase identification results, are seen regardless of the films' thickness. We note that the (111)

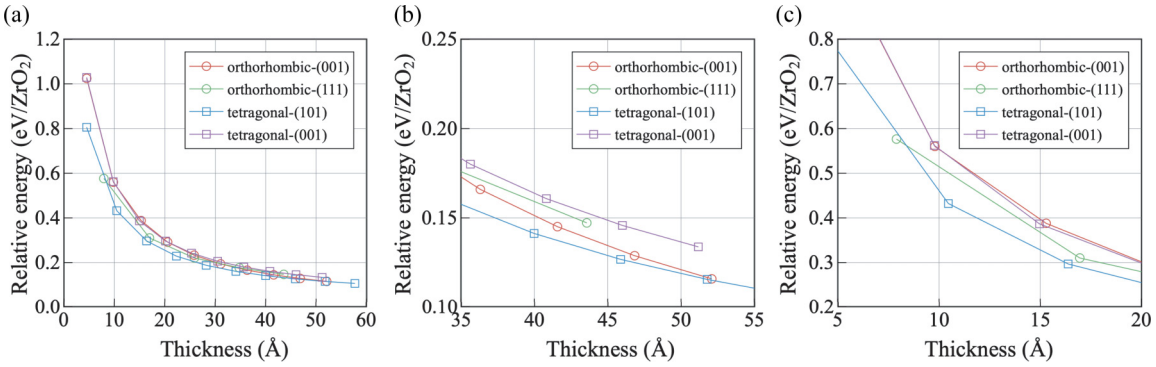

FIG. 4. (a) Relative structural energy of the tetragonal and orthorhombic ZrO_2 membrane models to the bulk orthorhombic one as a function of the thickness. (b), (c) Magnified views in the thickness region around (b) 50 Å and (c) 10 Å.

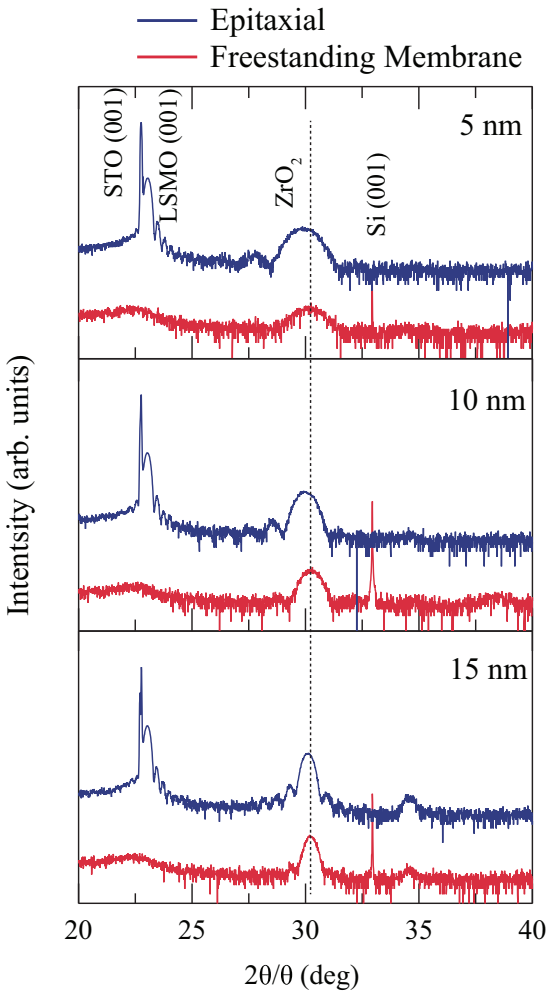

FIG. 5. X-ray $2\theta/\theta$ patterns for epitaxial ZO films and exfoliated ZO membranes. The dashed line marks the positions of the prominent diffraction peaks at 2θ to 30° for the freestanding membranes.

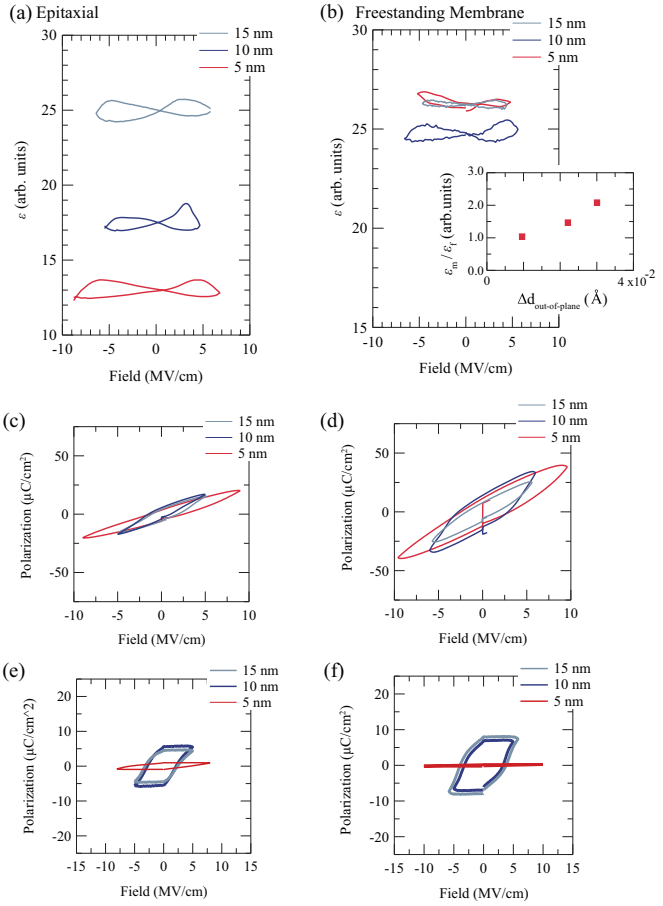

FIG. 6. Dielectric and ferroelectric properties of epitaxial ZO films and freestanding ZO membranes. (a), (b): ε-E curves for 5, 10, and 15-nm-thick (a) epitaxial ZO films and (b) freestanding ZO membranes. The inset in (b) shows the ratio of membrane' ε (ε_m) to film' ε (ε_f) as a function of the changes in the out-of-plane distance between the membrane and epitaxial film ($\Delta d_{out} = d_{111\_membranes} - d_{111\_film}$). (c), (d) P-E loops for 5, 10, and 15 nm-thick (c) epitaxial ZO films and (d) freestanding ZO membranes. (e), (f) PUND results for 5, 10 and 15-nm-thick (e) epitaxial ZO films and (d) freestanding ZO membranes. P-E and PUND results are obtained with the measurement frequency of 1 kHz.

reflection of the tetragonal phase should appear at $2\theta \sim 40°$, but no reflections are seen in such 2θ region. Also, no Zr arrangement corresponding to the rhombohedral structure is observed from the HAADF-STEM images. Therefore, the (111)-oriented tetragonal and rhombohedral structures are excluded from the candidates for peak assignment. Although additional reflection at 2θ to 34°, which can be indexed as (002) of the orthorhombic or tetragonal phase [38,39], is seen for the 15-nm-thick films, no reflections originating from the most stable monoclinic phase, whose (-111) reflection would appear at 2θ to 28° [39], are seen for any of the ZO films studied here. It should be noted that the main reflections (at 2θ to 30°) of the epitaxial ZO films shift toward the higher 2θ region as thickness increases, implying that substrate-induced compressive strain is possibly relaxed more in the thicker films and, as a result, the films' lattice (d_{out}) shrinkages along the out-of-plane direction decrease from 2.99 Å for the 5-nm-thick film to 2.96 Å for the 15-nm-thick one.

Freestanding ZO membranes transferred on SiO_2-coated Si wafers exhibit essentially the same diffraction profiles as those of ZO epitaxial films, as shown in Fig. 5. The observations indicate that ZO membranes can maintain their metastable polymorph structures without external strain, which is in close agreement with previous reports that HZO crystalline membranes can sustain their metastable polymorphs [9–11]. Interestingly, the reflection positions of ZO membranes (2θ to 30°) are thickness-independent (marked by a dashed line), giving a d_{out} of 2.95 Å, in contrast to those of the ZO epitaxial films, whose d_{out} depends on their thickness. The shrinkage in d_{out} for the freestanding membranes might be attributed to the strain relaxation associated with the exfoliation of ZO epitaxial layers.

V. DIELECTRIC AND FERROELECTRIC PROPERTIES OF ZrO_2 MEMBRANES

Figure 6 summarizes the electric-field dependence of the dielectric constant ε and polarization of ZO epitaxial films and membranes. Figures 6(a) and 6(b) show the electric-field

dependence of the dielectric constant ε for epitaxial (ε_f) and freestanding samples (ε_m). The ε_f is thickness-dependent and increases from 13 for the 5-nm-thick film to 25 for the 15-nm-thick one. In contrast, the ε_m is almost thickness-independent and as large as 25. The electric-field dependence of the dielectric loss for the epitaxial (ε_f) and freestanding samples (ε_m) are shown in Fig. S7 [25], ensuring that the contribution of leakage currents to the measured ε is tiny. The inset in Fig. 6(b) plots the ratio of ε_m to ε_f as a function of the changes in the out-of-plane distance between the membrane and epitaxial film ($\Delta d_{out} = d_{111\_membranes} - d_{111\_film}$). The $\varepsilon_m/\varepsilon_f$ increases monotonically with the increase of Δd_{out}. Given that thinner ZO epitaxial films accumulate more substrate-induced strain, our observations in ε-E indicate that the substrate-induced strain strongly influences the dielectric properties of ZO layers. It should be mentioned that, as shown in Fig. S8 [25], the dielectric constants measured for capacitor structures consisting of 10-nm-thick membranes and various bottom electrodes such as Au, LSMO, and $SrRuO_3$ are around 25, independent of the type of the bottom electrode (Fig. S8 [25]), indicating that the measured ε (capacitance) is contributed mainly from ZO layer and interfacial contribution is small. The increased ε of the ZO membranes can be attributed to the change of d_{out}, which is considered to stem from the relaxation of substrate-induced epitaxial strain and clamping effects. Similar increases in dielectric constants after the release of strain and clamping effects are reported for ferroelectric and antiferroelectric films [40,41].

The P-E loops in Figs. 6(c) and 6(d) and PUND loops obtained with triangular pulses of electric fields in Figs. 6(e) and 6(f) show that the 5-nm-thick film and membrane have no polarization while the 10- and 15-nm-thick films and membranes have a switchable polarization of around $5 \sim 7\,\mu C/cm^2$, which are further confirmed from I-E curves shown in Fig. S9 [25]. These observations indicate that the 5-nm-thick samples consisting of the nonpolar tetragonal structure are paraelectric and hardly undergo field-induced structural changes to a polar structural phase like the orthorhombic one. On the other hand, for samples thicker than 10 nm, in which the tetragonal and orthorhombic phases coexist, the observed polarization stems either from the polar orthorhombic phase or from a field-induced tetragonal-to-orthorhombic transformation that would be facilitated with the structural phase coexistence. It might be interesting to point out that the coercive fields of the membranes, which can be determined from I-E curves in Fig. S9 [25], are slightly larger than those of epitaxial films, while the remnant polarizations remain almost unchanged between films and membranes, implying that the epitaxial strain possibly facilitates polarization switching and field-induced structural transformations.

Finally, we point out that ultrathin ZO membranes with the nonpolar tetragonal structure are promising for energy storage applications. Figures 7(a) and 7(b) show P-E hysteresis loops with various maximum electric fields for the 5-nm-thick ZO membranes and the energy storage density (ESD), obtained from the P-E hysteresis loops [42]. Being beneficial from the high dielectric constant and the high breakdown field of the 5-nm-thick membranes, the ESD of our ZO-membrane-based capacitors is as large as 60 J/cm^3 with an efficiency as high as 65% and reaches 104 J/cm^3 at maximum with a lower

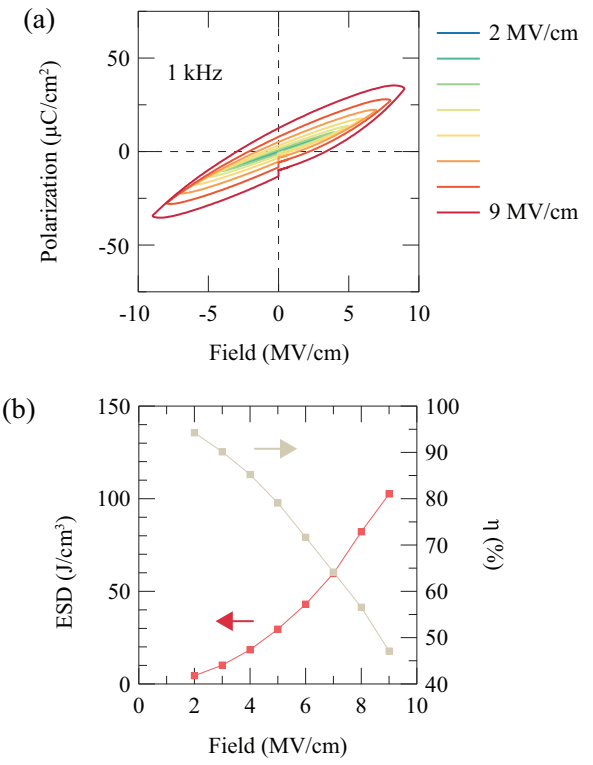

FIG. 7. Energy storage performance for 5-nm-thick ZO membrane. (a) P-E loops obtained under various maximum electrical fields. (b) Energy storage density and efficiency obtained from P-E loops in (a).

efficiency of 47% due to hysteresis loss. It should be noted that the ESD for the 5-nm-thick epitaxial thin films, calculated based on the P-E loops in Fig. 6(c), reaches only 70 J/cm^3 at the maximum electrical field of 9 MV/cm. In addition, the observed EDS for the membrane is superior to those for other binary-oxide-based capacitors (70 J/cm^3 or lower) [43–52], validating the potential application of the ZO membranes for dielectric energy storage.

VI. SUMMARY

We fabricated ultrathin ZO membranes with metastable crystal structures by exfoliating ZO epitaxial films from LSMO-buffered STO substrates and investigated structural and electrical properties. We find that ZO membranes can maintain metastable structures without external support and that their grains with the metastable nonpolar tetragonal structure in ZO membranes undergo structural relaxation to grains with the metastable polar orthorhombic structure with increasing thickness. In addition, the dielectric constant of the tetragonal ZO is found to be susceptible to the change of d_{out}, which is primarily related to the strain accumulated in the ZO layer. When the substrate-induced strain and clamping effects in the ZO layers are relaxed, the dielectric constant of the ZO membranes increases while high breakdown fields are maintained, highlighting their potential application for energy storage capacitors.

ACKNOWLEDGMENTS

This work was partly supported by Grants-in-Aid for Scientific Research (Grants No. 21H01810, No. 23KJ1239, No. 23H05457, No. 24H01190, and No. 22KJ3209) and by grants for the Integrated Research Consortium on Chemical Sciences and the International Collaborative Research Program of the Institute for Chemical Research in Kyoto University from the Ministry of Education, Culture, Sports, Science, and Technology (MEXT) of Japan. The work was also supported by the Japan Science and Technology Agency (JST) as part of PRESTO, Grant No. JPMJPR24H3, and Adopting Sustainable Partnerships for Innovative Research Ecosystem (ASPIRE), Grants No. JPMJAP2312 and No. JPMJAP2314. The authors acknowledge the use of instruments and scientific and technical assistance at the Monash Centre for Electron Microscopy (MCEM), Monash University, the Victorian Node of Microscopy Australia. This research used equipment funded by the Australian Research Council (Grant No. LE0454166). The work was also supported by The Samco Foundation.

YF.S. and D.K. conceived the idea. YF.S. and L.X. prepared the samples and YF.S. performed the XRD and electrical characterization under the instruction of TA.Y., TO.Y., and D.K. The theoretical calculation was performed by K.S., and S.K., K.O. performed the STEM observations and structural analysis. D.K. and Y.S. supervised the project. All the authors contributed to writing and discussing the manuscript.

DATA AVAILABILITY

The data that support the findings of this article are not publicly available upon publication because it is not technically feasible and/or the cost of preparing, depositing, and hosting the data would be prohibitive within the terms of this research project. The data are available from the authors upon reasonable request.

[1] S. S. Hong, J. H. Yu, D. Lu, A. F. Marshall, Y. Hikita, Y. Cui, and H. Y. Hwang, Two-dimensional limit of crystalline order in perovskite membrane films, Sci. Adv. **3**, eaao5173 (2017).

[2] D. Lu, D. J. Baek, S. S. Hong, L. F. Kourkoutis, Y. Hikita, and H. Y. Hwang, Synthesis of freestanding single-crystal perovskite films and heterostructures by etching of sacrificial water-soluble layers, Nat. Mater. **15**, 1255 (2016).

[3] D. Ji *et al.*, Freestanding crystalline oxide perovskites down to the monolayer limit, Nature (London) **570**, 87 (2019).

[4] Z. Chen, B. Y. Wang, B. H. Goodge, D. Lu, S. S. Hong, D. Li, L. F. Kourkoutis, Y. Hikita, and H. Y. Hwang, Freestanding crystalline $YBa_2Cu_3O_{7-x}$ heterostructure membranes, Phys. Rev. Mater. **3**, 060801 (2019).

[5] S. S. Hong *et al.*, Extreme tensile strain states in $La_{0.7}Ca_{0.3}MnO_3$ membranes, Science **368**, 71 (2020).

[6] K. Eom, M. Yu, J. Seo, D. Yang, H. Lee, J.-W. Lee, P. Irvin, S. H. Oh, J. Levy, and C.-B. Eom, Electronically reconfigurable complex oxide heterostructure freestanding membranes, Sci. Adv. **7**, eabh1284 (2021).

[7] B. Peng *et al.*, Phase transition enhanced superior elasticity in freestanding single-crystalline multiferroic $BiFeO_3$ membranes, Sci. Adv. **6**, eaba5847 (2020).

[8] G. Sánchez-Santolino *et al.*, A 2D ferroelectric vortex pattern in twisted $BaTiO_3$ freestanding layers, Nature (London) **626**, 529 (2024).

[9] H. Zhong *et al.*, Large-scale $Hf_{0.5}Zr_{0.5}O_2$ membranes with robust ferroelectricity, Adv. Mater. **34**, 2109889 (2022).

[10] Y. Shen, K. Ooe, X. Yuan, T. Yamada, S. Kobayashi, M. Haruta, D. Kan, and Y. Shimakawa, Ferroelectric freestanding hafnia membranes with metastable rhombohedral structure down to 1-nm-thick, Nat. Commun. **15**, 4789 (2024).

[11] Y.-C. Liu, B.-C. Chen, C.-C. Wei, S.-Z. Ho, Y.-D. Liou, P. Kaur, Rahul, Y.-C. Chen, and J.-C. Yang, Thickness-dependent ferroelectricity in freestanding $Hf_{0.5}Zr_{0.5}O_2$ membranes, ACS Appl. Electron. Mater. **6**, 8617 (2024).

[12] B. Xu *et al.*, Strain as a global factor in stabilizing the ferroelectric properties of ZrO_2, Adv. Funct. Mater. **34**, 2311825 (2024).

[13] K. Chae *et al.*, Local epitaxial templating effects in ferroelectric and antiferroelectric ZrO_2, ACS Appl. Mater. Interfaces **14**, 36771 (2022).

[14] A. P. S. Crema *et al.*, Ferroelectric orthorhombic ZrO_2 thin films achieved through nanosecond laser annealing, Adv. Sci. **10**, 2207390 (2023).

[15] R. Materlik, C. Künneth, and A. Kersch, The origin of ferroelectricity in $Hf_{1-x}Zr_xO_2$: A computational investigation and a surface energy model, J. Appl. Phys. **117**, 134109 (2015).

[16] A. El Boutaybi *et al.*, Ferroelectricity in epitaxial tetragonal ZrO_2 thin films, Adv. Electron. Mater. **10**, 2300516 (2024).

[17] A. El Boutaybi, T. Maroutian, L. Largeau, S. Matzen, and P. Lecoeur, Stabilization of the epitaxial rhombohedral ferroelectric phase in ZrO_2 by surface energy, Phys. Rev. Mater. **6**, 074406 (2022).

[18] J. P. B. Silva, R. F. Negrea, M. C. Istrate, S. Dutta, H. Aramberri, J. Íñiguez, F. G. Figueiras, C. Ghica, K. C. Sekhar, and A. L. Kholkin, Wake-up free ferroelectric rhombohedral phase in epitaxially strained ZrO_2 thin films, ACS Appl. Mater. Interfaces **13**, 51383 (2021).

[19] M. Hoffmann *et al.*, Antiferroelectric negative capacitance from a structural phase transition in zirconia, Nat. Commun. **13**, 1228 (2022).

[20] S. E. Reyes-Lillo, K. F. Garrity, and K. M. Rabe, Antiferroelectricity in thin-film ZrO_2 from first principles, Phys. Rev. B **90**, 140103 (2014).

[21] X. Li *et al.*, Polarization switching and correlated phase transitions in fluorite-structure ZrO_2 nanocrystals, Adv. Mater. **35**, 2207736 (2023).

[22] X. Li *et al.*, Ferroelastically protected reversible orthorhombic to monoclinic-like phase transition in ZrO_2 nanocrystals, Nat. Mater. **23**, 1077 (2024).

[23] B. Allouche, H. J. Hwang, T. J. Yoo, and B. H. Lee, A negative electrocaloric effect in an antiferroelectric zirconium dioxide thin film, Nanoscale **12**, 3894 (2020).

[24] S. Starschich and U. Böttger, Doped ZrO_2 for future lead free piezoelectric devices, J. Appl. Phys. **123**, 044101 (2018).

[25] See Supplemental Material at http://link.aps.org/supplemental/10.1103/PhysRevMaterials.9.024411 for details of phase identification for epitaxial films and membranes of ZrO_2, details of dielectric constants and polarizations for epitaxial films and membranes of ZrO_2, and details of our first-principles calculations.

[26] G. Kresse and J. Furthmüller, Efficiency of *ab-initio* total energy calculations for metals and semiconductors using a plane-wave basis set, Comput. Mater. Sci. **6**, 15 (1996).

[27] G. Kresse and J. Furthmüller, Efficient iterative schemes for *ab initio* total-energy calculations using a plane-wave basis set, Phys. Rev. B **54**, 11169 (1996).

[28] G. Kresse and D. Joubert, From ultrasoft pseudopotentials to the projector augmented-wave method, Phys. Rev. B **59**, 1758 (1999).

[29] J. P. Perdew, A. Ruzsinszky, G. I. Csonka, O. A. Vydrov, G. E. Scuseria, L. A. Constantin, X. Zhou, and K. Burke, Restoring the density-gradient expansion for exchange in solids and surfaces, Phys. Rev. Lett. **100**, 136406 (2008).

[30] L. Bengtsson, Dipole correction for surface supercell calculations, Phys. Rev. B **59**, 12301 (1999).

[31] D. Pesquera *et al.*, Beyond substrates: Strain engineering of ferroelectric membranes, Adv. Mater. **32**, 2003780 (2020).

[32] R. Xu *et al.*, Size-induced ferroelectricity in antiferroelectric oxide membranes, Adv. Mater. **35**, 2210562 (2023).

[33] R. Frisenda, E. Navarro-Moratalla, P. Gant, D. P. D. Lara, P. Jarillo-Herrero, R. V. Gorbachev, and A. Castellanos-Gomez, Recent progress in the assembly of nanodevices and van der Waals heterostructures by deterministic placement of 2D materials, Chem. Soc. Rev. **47**, 53 (2018).

[34] S. Estandía, N. Dix, M. F. Chisholm, I. Fina, and F. Sánchez, Domain-matching epitaxy of ferroelectric $Hf_{0.5}Zr_{0.5}O_2$ (111) on $La_{2/3}Sr_{1/3}Mn_3$ (001), Cryst. Growth Des. **20**, 3801 (2020).

[35] S. Shi *et al.*, Interface-engineered ferroelectricity of epitaxial $Hf_{0.5}Zr_{0.5}O_2$ thin films, Nat. Commun. **14**, 1 (2023).

[36] G. Fadda, G. Zanzotto, and L. Colombo, First-principles study of the effect of pressure on the five zirconia polymorphs. I. Structural, vibrational, and thermoelastic properties, Phys. Rev. B **82**, 064105 (2010).

[37] B. Xu, P. D. Lomenzo, A. Kersch, T. Mikolajick, and U. Schroeder, Influence of Si-doping on 45 nm thick ferroelectric ZrO_2 films, ACS Appl. Electron. Mater. **4**, 3648 (2022).

[38] P. D. Lomenzo, M. Materano, T. Mittmann, P. Buragohain, A. Gruverman, T. Kiguchi, T. Mikolajick, and U. Schroeder, Harnessing phase transitions in antiferroelectric ZrO_2 using the size effect, Adv. Electron. Mater. **8**, 2100556 (2022).

[39] J. Müller, T. S. Böscke, U. Schröder, S. Mueller, D. Bräuhaus, U. Böttger, L. Frey, and T. Mikolajick, Ferroelectricity in simple binary ZrO_2 and HfO_2, Nano Lett. **12**, 4318 (2012).

[40] F. Griggio, S. Jesse, A. Kumar, O. Ovchinnikov, H. Kim, T. N. Jackson, D. Damjanovic, S. V. Kalinin, and S. Trolier-McKinstry, Substrate clamping effects on irreversible domain wall dynamics in lead zirconate titanate thin films, Phys. Rev. Lett. **108**, 157604 (2012).

[41] Y. Guo *et al.*, Remarkable flexibility in freestanding single-crystalline antiferroelectric $PbZrO_3$ membranes, Nat. Commun. **15**, 4414 (2024).

[42] Y. Yu *et al.*, Structure-evolution-designed amorphous oxides for dielectric energy storage, Nat. Commun. **14**, 3031 (2023).

[43] Y. Wang, Y. Wang, H. Zeng, and X. Wei, Ultra-high energy storage density of transparent capacitors based on linear dielectric ZrO_2 thin films with the thickness scaled up to hundreds nanometers, Appl. Phys. Lett. **120**, 023904 (2022).

[44] Y. He, G. Zheng, X. Wu, W.-J. Liu, D. W. Zhang, and S.-J. Ding, Superhigh energy storage density on-chip capacitors with ferroelectric $Hf_{0.5}Zr_{0.5}O_2$/antiferroelectric $Hf_{0.25}Zr_{0.75}O_2$ bilayer nanofilms fabricated by plasma-enhanced atomic layer deposition, Nanoscale Adv. **4**, 4648 (2022).

[45] M. Hoffmann, F. P. G. Fengler, B. Max, U. Schroeder, S. Slesazeck, and T. Mikolajick, Negative capacitance for electrostatic supercapacitors, Adv. Energy Mater. **9**, 1901154 (2019).

[46] S.-H. Yi, H.-C. Lin, and M.-J. Chen, Ultra-high energy storage density and scale-up of antiferroelectric $TiO_2/ZrO_2/TiO_2$ stacks for supercapacitors, J. Mater. Chem. A **9**, 9081 (2021).

[47] A. Payne, O. Brewer, A. Leff, N. A. Strnad, J. L. Jones, and B. Hanrahan, Dielectric, energy storage, and loss study of antiferroelectric-like Al-doped HfO_2 thin films, Appl. Phys. Lett. **117**, 221104 (2020).

[48] K. D. Kim, Y. H. Lee, T. Gwon, Y. J. Kim, H. J. Kim, T. Moon, S. D. Hyun, H. W. Park, M. H. Park, and C. S. Hwang, Scale-up and optimization of HfO_2-ZrO_2 solid solution thin films for the electrostatic supercapacitors, Nano Energy **39**, 390 (2017).

[49] J. P. B. Silva, J. M. B. Silva, K. C. Sekhar, H. Palneedi, M. C. Istrate, R. F. Negrea, C. Ghica, A. Chahboun, M. Pereira, and M. J. M. Gomes, Energy storage performance of ferroelectric ZrO_2 film capacitors: Effect of HfO_2 : Al_2O_3 dielectric insert layer, J. Mater. Chem. A **8**, 14171 (2020).

[50] F. Ali, X. Liu, D. Zhou, X. Yang, J. Xu, T. Schenk, J. Müller, U. Schroeder, F. Cao, and X. Dong, Silicon-doped hafnium oxide anti-ferroelectric thin films for energy storage, J. Appl. Phys. **122**, 144105 (2017).

[51] P. D. Lomenzo, C.-C. Chung, C. Zhou, J. L. Jones, and T. Nishida, Doped $Hf_{0.5}Zr_{0.5}O_2$ for high efficiency integrated supercapacitors, Appl. Phys. Lett. **110**, 232904 (2017).

[52] M. H. Park, H. J. Kim, Y. J. Kim, T. Moon, K. D. Kim, and C. S. Hwang, Thin $Hf_xZr_{1-x}O_2$ films: A new lead-free system for electrostatic supercapacitors with large energy storage density and robust thermal stability, Adv. Energy Mater. **4**, 1400610 (2014).